FULL PAPER

# Highly Elastic and Conductive N-Doped Monolithic Graphene Aerogels for Multifunctional Applications

*In Kyu Moon, Seonno Yoon, Kyoung-Yong Chun,\* and Jungwoo Oh\**

The simple synthesis of ultralow-density ($\approx$2.32 mg cm$^{-3}$) 3D reduced graphene oxide (rGO) aerogels that exhibit high electrical conductivity and excellent compressibility are described herein. Aerogels are synthesized using a combined hydrothermal and thermal annealing method in which hexamethylenetetramine is employed as a reducer, nitrogen source, and graphene dispersion stabilizer. The N-binding configurations of rGO aerogels increase dramatically, as evidenced by the change in pyridinic-N/quaternary-N ratio. The conductivity of this graphene aerogel is $\approx$11.74 S m$^{-1}$ at zero strain, whereas the conductivity at a compressive strain of $\approx$80% is $\approx$704.23 S m$^{-1}$, which is the largest electrical conductivity reported so far in any 3D sponge-like low-density carbon material. In addition, the aerogel has excellent hydrophobicity (with a water contact angle of 137.4°) as well as selective absorption for organic solvents and oils. The compressive modulus (94.5 kPa; $\rho \approx$ 2.32 mg cm$^{-3}$) of the rGO aerogel is higher than that of other carbon-based aerogels. The physical and chemical properties (such as high conductivity, elasticity, high surface area, open pore structure, and chemical stability) of the aerogel suggest that it is a viable candidate for the use in energy storage, electrodes for fuel cells, photocatalysis, environmental protection, energy absorption, and sensing applications.

## 1. Introduction

During the past five years, 3D graphene[1] and reduced graphene oxide (rGO)[2] nanostructured aerogels have been extensively investigated. These materials have potential for use in next-generation technology for flexible energy storage and generation[3] as well as use in energy cushions,[4] sensors,[1,5]

Dr. I. K. Moon
Yonsei Institute of Convergence Technology
Yonsei University
Yeonsu-gu, Incheon 21983, Republic of Korea
S. Yoon, Prof. J. Oh
School of Integrated Technology and
Yonsei Institute of Convergence Technology
Yonsei University
Yeonsu-gu, Incheon 21983, Republic of Korea
E-mail: jungwoo.oh@yonsei.ac.kr
Dr. K.-Y. Chun
Development Group for Creative Research Engineers
of Convergence Mechanical System
Korea University
Seongbuk-gu, Seoul 02841, Republic of Korea
E-mail: kychun@gmail.com

actuators,[6] and absorbers of environmental pollution.[2,7] Among graphene-based materials, graphene oxides (GOs) can be described as "up-and-coming" material candidates because they are thin, light, strong, environmentally friendly, and flexible. They also have high surface area, excellent mechanical–chemical properties, and the ability to conduct electricity within 2D nanostructures. Many research groups[8] have reported the simple preparation of rGO aerogels from GO solution by hydrothermal and freeze-drying methods or etching methods, employing a spherical template/GO composite. The microstructural features of rGO aerogels make them some of the most promising building blocks for energy-related and environmental applications. This is because these features can greatly improve working-volume deformability, can form a multidimensional conduction network, and can provide 3D interfacing or intercalation with other system components (e.g., electrolytes, reactants).[8] However, the performance and diversity of such graphene aerogel conductors are limited by the lack of a sufficient compressive modulus (that is, they are fragile and collapse under stress).[4,9] Aerogels usually have an extremely low density due to their relatively high rigidity and/or a rather low electrical conductivity (e.g., 0.12 S m$^{-1}$ with a density of 5.10 mg cm$^{-3}$).[10] These properties can result from an incomplete reduction if mild chemical reducing conditions are employed without thermal annealing. Zhao et al.[11] reported the development of a compression-tolerant rGO sponge supercapacitor with a polypyrrole coating, which is conductive and provides mechanical reinforcement. This work showed that the use of rGO sponges in conjunction with other materials can overcome some of the shortcomings of monolithic rGO sponges. Recently, Wu et al.[12] fabricated a spongy graphene material (density = 1.15 mg cm$^{-3}$; conductivity = 0.37 S m$^{-1}$) that showed compressive elasticity and a near-zero Poisson's ratio by using a solvo-thermal reaction and thermal annealing. The primary remaining challenge is the synthesis of additive-free monolithic rGO aerogels that preserve the low density, high conductivity, and good elasticity inherent in GO nanosheets.

In this article, we describe the development of a facile approach for fabricating support-free monolithic nitrogen (N)-doped rGO aerogels using a simple hydrothermal method employing hexamethylenetetramine (HMTA) as a stabilizer

www.MaterialsViews.com

ADVANCED
FUNCTIONAL
MATERIALS
www.afm-journal.de

FULL PAPER

and nitrogen source. These N-doped rGO aerogels have both good compressibility and electrical conductivity as well as an extremely low density ($\approx$2.32 mg cm$^{-3}$). Our rGO aerogel showed 11.74–704.23 S m$^{-1}$ conductivity when uniaxial compression was increased from zero strain to 80% strain. This approach leads to a simplified, lightweight architecture that allows for larger mass loading of guest materials. Furthermore, our novel graphene aerogel has unique electrical and mechanical properties due to the presence of N-doped monolithic graphene, and these aerogels may be suitable for a wide variety of applications.

## 2. Results and Discussion

**Figure 1**a illustrates the preparation procedure for the 3D porous rGO aerogels. Briefly, the target nitrogen-doped monolithic rGO aerogel was prepared through a two-step approach. First, the rGO aerogel (denoted as rGO$_{hydro}$ aerogel) was synthesized successfully through a simultaneous self-assembly and reduction process. In this process, we used HMTA as a reducer and a nitrogen source. HMTA was also used to stabilize the graphene dispersion through electrostatic interactions. The obtained rGO hydrogel was taken out of the reactor and subsequently freeze-dried for 48 h. To improve the quality of the aerogel, the rGO$_{hydro}$ aerogel was thermally annealed in a 10$^{-3}$ Torr atmosphere at 1000 °C for 3 h (heating rate = 1 °C min$^{-1}$), yielding a sample referred to as the rGO$_{thermal}$ aerogel. In Figure 1b, rGO$_{thermal}$ aerogels show a striking recovery of their original shape under high compression ($\varepsilon > 80\%$) without collapsing (Movie 1 and 2, Supporting Information). The obtained rGO aerogel was highly elastic (without using any linkage

additives or polymer reinforcement) and was easily converted into compressible rGO$_{thermal}$ via thermal treatment. The synthesized macroporous rGO$_{hydro}$ and rGO$_{thermal}$ aerogels were ultra-lightweight with densities ($\rho$) of $\approx$3.20 mg cm$^{-3}$ and $\approx$2.32 mg cm$^{-3}$, respectively (see Figure 1a).

HMTA not only served as a nitrogen dopant and reducing agent in the hydrothermal reaction process, but also played a role as modifier in the self-assemble formation process of the porous hydrogels. In the majority of cases, it remains in the design and synthesis of these aerogels of macrostructures due to the limited knowledge of the sol–gel chemistry between graphene oxides and/or crosslinking agents.[13] During hydrolysis in an aqueous solution, however, HMTA releases ammonia and hydroxide ion.[14] An abundance of hydroxide ion and ammonia can reduce graphene oxide to rGO by removing oxygen-containing functional groups[15] and can simultaneously introduce nitrogen atoms into the graphene skeleton by substituting carbon atoms,[16] respectively.

The following reactions might occur in solution above 60 °C[14]

$$C_6H_{12}N_4 \,(HMTA) + 6H_2O \rightarrow 6HCHO + 4NH_3 \tag{1}$$

$$NH_3 + H_2O \rightarrow NH_4^+ + OH^- \tag{2}$$

And also, the excess ammonia in GO aqueous-formed stable colloids through electrostatic repulsion of negatively charged GO sheets.[17] Considering the simple reaction system containing only GO and HMTA, we infer that the excess HMTA could act as a capping reagent in stabilizing as-prepared rGO sheets.

As-prepared rGO aerogels were characterized by a variety of methods including X-ray diffraction (XRD), scanning electron microscopy (SEM), Raman spectroscopy, and X-ray
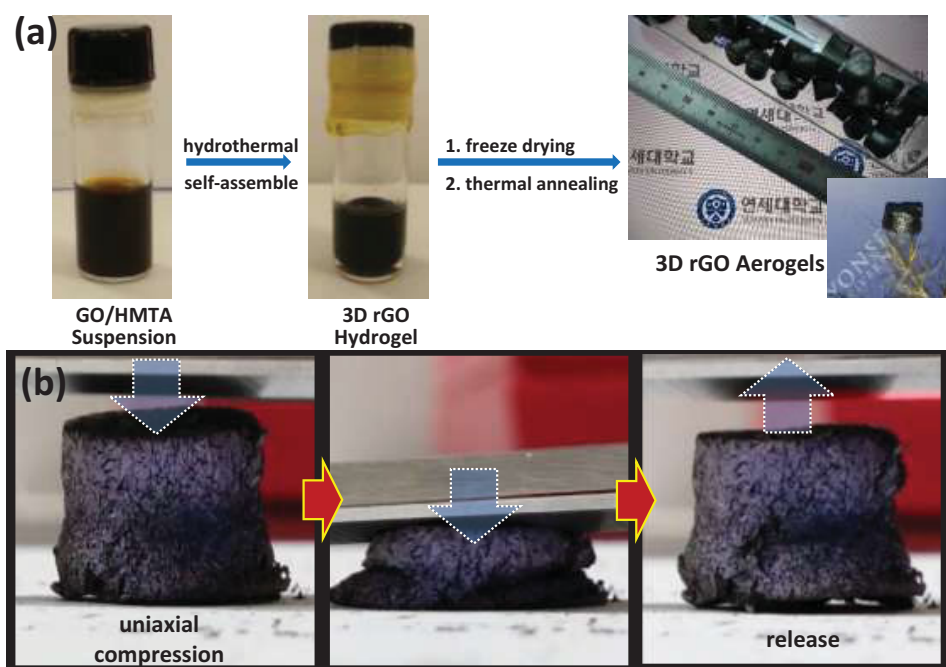


**Figure 1.** a) Schematic representation and photo images of the synthesis procedure for ultralight N-doped rGO$_{thermal}$ aerogels with a density of $\approx$2.32 mg cm$^3$. b) Snapshots of the compressibility of the rGO$_{thermal}$ aerogel.

**ADVANCED
FUNCTIONAL
MATERIALS**

www.afm-journal.de

**FULL PAPER**
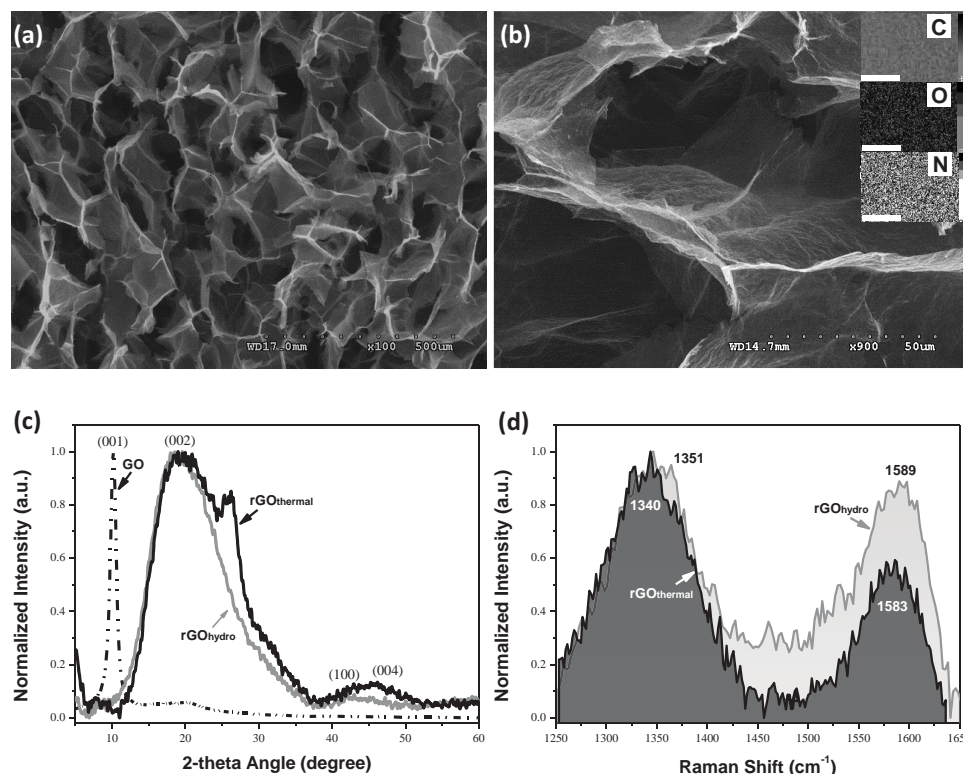
*Materials Views*

www.MaterialsViews.com

**Figure 2.** a) The XRD patterns of GO, rGO$_{hydro}$, and rGO$_{thermal}$ aerogels. b) Raman spectra of rGO$_{hydro}$ and rGO$_{thermal}$ aerogels with a laser excitation at 532 nm (2.33 eV). c,d) Low- and high-magnification SEM images of rGO thermal aerogels. Inset in (b) shows EDX elemental maps of carbon (gray), oxygen (light gray), and nitrogen (white) (scale bar = 3 mm).

photoelectron spectroscopy (XPS). The XRD pattern of rGO$_{hydro}$ (**Figure 2**a) showed a broad (002) peak at about 18°–20°, which corresponds to an interlayer distance of approximately 4.9–4.4 Å ($d_{002}$) (in GO a $2\theta$ of ≈10.93° corresponds to an interlayer distance of ≈8.08 Å ($d_{002}$)). This distance is the largest value ever reported in the literature and is due to both the cage-like (nearly spherical) shape of HMTA as well as the remaining oxygen-functional groups in the rGO nanosheets, which occupy the interlayer galleries of the rGO sheets. The rGO$_{thermal}$ aerogel shows a broad peak at a position similar to that of the rGO$_{hydro}$ aerogel. In addition, a new broad diffraction peak at $2\theta \approx 42°$ and 49° appeared, corresponding to the planes (100) and (004), respectively. The (002) and (004) peaks correspond to parallel graphene layers. The (100) peak characterize the 2D in-plane symmetry along the graphene layers.[18] A broad shoulder at $2\theta \approx 26°$ ($d_{002} = 3.4$ Å) was also observed closer to the (002) graphite peak of 3.36 Å.[19] This result suggested that the rGO$_{thermal}$ aerogel was well ordered and had some 2D sheets of graphite without oxygen functional groups.

Representative Raman spectra of rGO aerogels using 532 nm laser excitation are shown in Figure 2b. The G-bands of the rGO$_{hydro}$ and rGO$_{thermal}$ aerogel appeared at 1589 and 1583 cm$^{-1}$, respectively. The downshift of the G-band in the rGO$_{thermal}$ aerogel can be attributed to sp$^2$ restoration during pyrolysis[20] and the incorporation of heteroatoms into the graphene structure.[21] The relative peak intensities of the G- and D-bands were $I_D/I_G = 1.12$ for the rGO$_{hydro}$ aerogel and $I_D/I_G = 1.66$ for the rGO$_{thermal}$ aerogel. The crystallite size ($L_a$)

can be determined according to the Tuinstra–Koening relation,[22] $L_a$ (nm) = $(2.4 \times 10^{-10})\lambda^4(I_D/I_G)^{-1}$ (where $\lambda$ is the Raman excitation wavelength). An $L_a$ of ≈11.58 nm was obtained for the rGO$_{thermal}$ aerogel, and this was smaller than that of the rGO$_{hydro}$ aerogel ($L_a \approx 17.16$ nm). This result can be attributed to a decrease in the average size of the sp$^2$ domains upon thermal reduction of the rGO$_{hydro}$ aerogel. In other words, the increased $I_D/I_G$ ratio probably resulted from the release of gases by decomposition of the remaining oxygen-functional groups and sp$^3$-hybridized carbon atoms during thermal annealing. Reduction may also have caused cracking of the in-plane C=C, resulting in the generation of more defects. Defects may also have resulted from the generation of smaller nanocrystalline graphene domains[23] and the incorporation of N-heteroatoms.[21,24]

The N-doped monolithic rGO$_{thermal}$ aerogels were imaged using SEM to determine the uniformity and microporous structure of the rGO layers (Figure 2c,d. Clearly, the open-pore walls in the foams are continuously cross-linked, forming an interconnected porous network between the rGO layers in each cell wall. This structure not only provides effective stacking of the graphene sheets with lateral sizes ranging from several hundred nanometers to several micrometers, but it also improves intersheet contact and provides large area-to-volume ratios. The rGO cells show a typical quasicork-like structure. Moreover, the graphene platelet walls are rather thin and wrinkled, indicating the efficient self-assembly of graphene nanosheets. Energy dispersive X-ray spectroscopy (EDX) elemental mapping of rGO$_{hydro}$ and rGO$_{thermal}$ aerogels shown in Figure S1 (Supporting Information) and the

www.MaterialsViews.com

ADVANCED
FUNCTIONAL
MATERIALS
www.afm-journal.de

FULL PAPER

inset of Figure 2d, respectively, indicates that a uniform distribution of N, C, and O atoms was present in the rGO aerogels. As shown in Figure S2 (Supporting Information), the obtained rGO$_{thermal}$ nanosheets include wrinkled and folded sheets.

As expected, the chemically N-doped rGO aerogels exhibit C 1s and N 1s peaks at ≈286 and ≈398 eV from XPS survey scan in Figure S3 (Supporting Information), respectively, because of the HMTA doping. As shown in **Figure 3**a,b, the C 1s core-level spectrum of the rGO aerogels was fitted using five component peaks with binding energies of 284.6, 285.9, 287.1, 288.5, and 290.0 eV. These are attributed to the contribution of sp$^2$ (284.6 and 290.0 eV) hybridized carbon, sp$^3$ hybridized carbons, C–O, C=O, and C(O)OH, respectively. After hydrothermal and thermal annealing of GO in the HMTA mixture, the O 1s peaks decreased significantly. The carbon-to-oxygen atomic ratio ($R_{C/O}$) was determined from the C 1s core-level spectra. The $R_{C/O}$ (≈31.12) of rGO$_{thermal}$ aerogel was a dramatically reduced as compared to the rGO$_{hydro}$ aerogel ($R_{C/O}$ ≈ 4.47) (see Tables S1 and S2 in the Supporting Information).

The characteristic N 1s peak is also present in both N-doped rGO aerogels. This N 1s peak can be deconvoluted into three main component peaks, representing pyridinic-nitrogen (N$_P$ at 398 eV), pyrrolic-nitrogen (N$_{PYR}$ at 399 eV), and quaternary-nitrogen (N$_Q$ at 401 eV); no chemisorbed nitrogen oxides were observed at ≈404–406 eV.[25] Their configurations are schematically described in Figure S4 (Supporting Information). N$_P$ and N$_Q$ heteroatoms within the rGO sheet show sp$^2$-hybridized bonding, while N$_{PYR}$ is sp$^3$ hybridized in a five-membered ring.[25] For the rGO$_{thermal}$ sponge, the area compositions of N$_P$, N$_Q$, and N$_{PYR}$ were 21.59%, 50.57%, and 21.85%, while these values for the rGO$_{hydro}$ aerogel were 3.21%, 60.23%, and 36.56%, respectively. The relative intensities of N$_P$/N$_Q$ in rGO$_{hydro}$ and rGO$_{thermal}$

aerogels were ≈0.05 and ≈0.43, indicating that the nitrogen atoms incorporated into the rGO aerogel are mainly in the form of quaternary nitrogen. After thermal annealing ($T$ = 1000 °C) of the rGO$_{hydro}$ aerogel, the percentage of N$_P$ increases significantly. In contrast, the percentage of N$_Q$ and N$_{PYR}$ decreased slightly due to the thermal stability of nitrogen derivatives within the graphitic structure.[25] N levels in both rGO$_{hydro}$ and rGO$_{thermal}$ aerogels were ≈7.7% and ≈3.63%, respectively. N-doping levels observed in our work are compared with reported N-doped graphene (doping level ≈1%–3%) materials made by thermal annealing, arc discharge, plasma, and chemical vapor deposition methods in Table S3 (Supporting Information).[26]

Wettability of the as-prepared both rGO$_{hydro}$ and rGO$_{thermal}$ aerogels was determined by measuring both water and oil contact angle (CA) (**Figure 4**a,b; Figure S5, Supporting Information). The synthesized rGO$_{hydro}$ and rGO$_{thermal}$ aerogels showed water contact angles of 131° to 144.5°, which are due to the decrease in the number of oxygen-functional groups of rGO sheets. These results are supported by XPS data, where the rGO$_{thermal}$ aerogel ($R_{C/O}$ ≈ 31.12 by XPS) exhibited fewer surface oxygen atoms than those of the rGO$_{hydro}$ aerogel ($R_{C/O}$ ≈ 4.47 by XPS). These results indicate that the rGO$_{thermal}$ aerogel is an ideal candidate for oil/solvent absorbents to clean oil/solvent spills in marine environments. Along these lines, Figure S6 (Supporting Information) presents an image of the combustion of gasoline absorbed by the aerogel.

The macro-, micro-, and mesoporous features of these aerogels were further confirmed by N$_2$ adsorption–desorption measurements (see Figure 4c). The surface areas of rGO$_{hydro}$ and rGO$_{thermal}$ aerogels, which were calculated by the Brunauer–Emmett–Teller (BET) equation using N$_2$ adsorption/desorption isotherms, were estimated to be 327.05 and 194.14 m$^2$ g$^{-1}$,
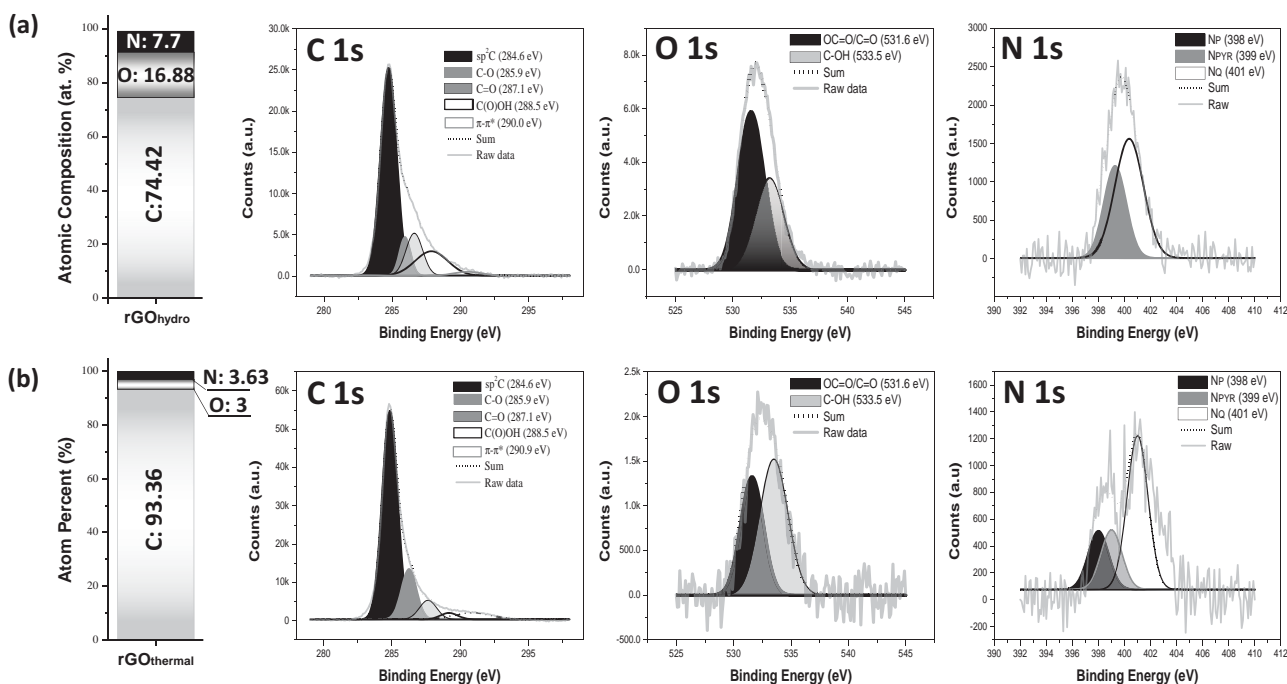


**Figure 3.** XPS high-resolution spectra of both a) rGO$_{hydro}$ and b) rGO$_{thermal}$ aerogels. The atomic percentages of C, O, and N in rGO aerogels were obtained from XPS data.

ADVANCED
FUNCTIONAL
MATERIALS

www.afm-journal.de
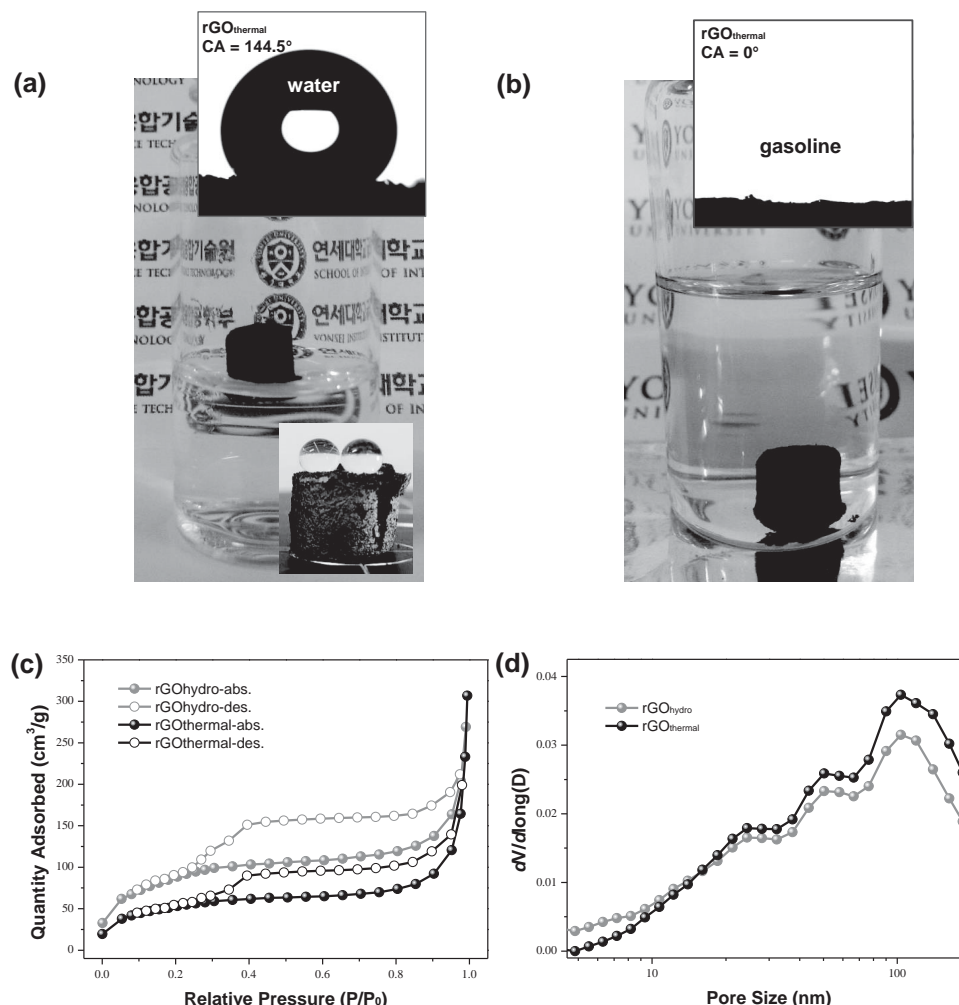
www.MaterialsViews.com

FULL PAPER

**Figure 4.** a,b) rGO thermal aerogel capability for organic absorption and wetting behavior. The rGO$_{thermal}$ aerogel floats when in contact with water. A water droplet forms a contact angle of 144.6° with the longitudinal section of the aerogel (inset: water droplets on a rGO$_{thermal}$ aerogel). The rGO$_{thermal}$ aerogel rapidly absorbs gasoline, filling the highly porous structure. c) N$_2$ adsorption/desorption isotherms and d) BJH pore-size distribution curves obtained from the adsorption branch of each rGO aerogel.

respectively. Figure 4d shows the pore-size distribution of the rGO$_{thermal}$ aerogel. As shown, a broad distribution centered at 2 nm and a broader distribution ranging from 10 to 110 nm were observed using the Barret–Joyner–Halenda (BJH) method.

Uniaxial compression and electrical conductivity results are provided in **Figure 5**a. Under an increased compressive loading, more contact area was created between rGO platelets in the 3D networks, thus decreasing the contact resistance. Upon unloading, the reverse occurred, which is reflected in the change of resistance. The conductivity ($\sigma$) of the rGO$_{thermal}$ aerogel at zero strain (aerogel density ≈2.32 mg cm$^{-3}$) was ≈11.74 S m$^{-1}$, whereas under compressive strain ($\varepsilon$) ≈ 80%, it was ≈704.23 S m$^{-1}$, which appears to be the largest electrical conductivity reported so far for any low-density 3D sponge-like carbon material.[1,4a,10,12,27–33] In contrast, the rGO$_{hydro}$ aerogel (density of ≈3.20 mg cm$^{-3}$) showed values of ≈0.13 S m$^{-1}$ at $\varepsilon$ ≈ 0% and 358.17 S m$^{-1}$ at $\varepsilon$ ≈ 80%.

Electrical conductivity was measured by using a four-probe method (see Figure S7 in the Supporting Information).

Figure 5a shows electric conductivity as a function of uniaxial compressive strain, which ranges from several S m$^{-1}$ to several hundreds of S m$^{-1}$. The conductivity changed dramatically only when the strain was larger than 60%. Increases in conductivity were also ascribed to densification or buckling between graphene platelet sheets, bridging of the cell wall under high strain ($\varepsilon > 60\%$), and higher degrees of interconnection within their highly porous structures. These mechanisms are consistent with the dynamic-SEM results (see Figure 5c; Figure S8 in the Supporting Information). When the rGO aerogel is compressed, its density $\rho$ increases as $\rho = \rho_0/(1 - \varepsilon)$, where $\rho_0$ is the initial density.[34] Results of calculations using this equation during the uniaxial compression with each aerogel density are shown in Figure 5b. The electrical conductivity of the rGO$_{thermal}$ aerogel was 15.65 S m$^{-1}$ at $\varepsilon$ ≈ 10%, which is over 42 times higher than values for graphene-based aerogels with similar densities after thermal annealing at 400 °C ($\sigma = 0.37$ S m$^{-1}$ at $\varepsilon$ ≈ 10% with a density of ≈1.15 mg cm$^3$) (see Figure 5b).[12]

www.MaterialsViews.com

ADVANCED
FUNCTIONAL
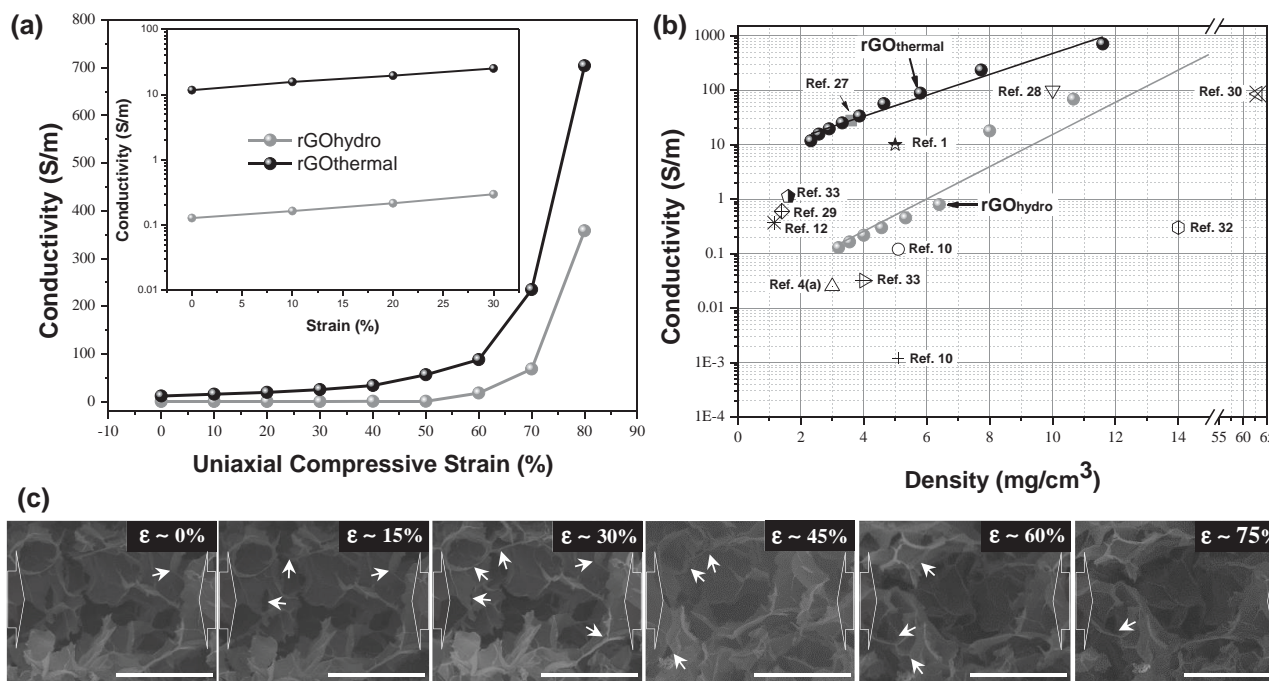MATERIALS
www.afm-journal.de

FULL PAPER

**Figure 5.** a) Electrical conductivity of both rGO aerogels when compressed along the axial direction. b) The electrical conductivity of both rGO aerogels as a function of density together with several low-density carbon materials reported in the literature. The line is a guide for the eyes. c) SEM images of loading states of rGO$_{thermal}$ aerogel under uniaxial compression (scale bar = 250 mm).

To better explain the change in conductivity of the rGO$_{thermal}$ aerogel with compression, SEM images of the rGO$_{thermal}$ aerogel within the range of 0% to ≈75% compressive strain were collected and compared (see Figure 5c). As expected, the SEM images in Figure 5c reveal deformation processes at various applied compressive strain levels. The original aerogel had many macropores, which inhibit electrical transport. As the images of the compressed rGO$_{thermal}$ aerogel show, the 3D graphene network became more compact and macropores disappeared. With increasing strain ($\varepsilon \approx 45\%$–75%), buckling or densification between cell walls and/or graphene platelet sheets increases, and many flat cells appear. All of these mechanisms result in an increase in the electrical conductivity of the aerogel. This result confirms the presence of a 3D conducting pathway throughout the macropore structure, which perfectly matches the electrical conductivity results.

We have done mechanical testing on rGO$_{hydro}$ and rGO$_{thermal}$ aerogels to study their compressive strength, compressibility, and recoverability (up to 50% strain). When an rGO aerogel is uniaxially compressed, it exhibits a porous-like response, i.e., the stress increases nonlinearly with strain up to the peak stress, and then follows a rapid unloading along a different stress–strain path, is responsible for the energy dissipation. **Figure 6**a,b and Movies 1 and 2 (Supporting Information) show a typical cyclic stress–strain curve of the rGO$_{hydro}$ and rGO$_{thermal}$ aerogels that the rGO$_{hydro}$ aerogels become stiffer after thermal annealing. This may be explained on the basis of the strongly interacting surface oxygen groups in rGO$_{hydro}$ sheets, the large pore size of interconnected rGO networks,[35] and the van der Waals interaction between graphene sheets in different reduction degrees. The curves show the typical features of porous material, with an initial linear elastic region ($\varepsilon < 40\%$–45%) at

relatively lower stress levels after the third cycle due to the high porosity and softness of the sponge, followed by compaction and a steep slope region at $\varepsilon > 40\%$–45% with rapidly rising stress because of the densification of aerogels (Figure 6a,b); it has been shown that rGO aerogels show a rapid increase in tangent modulus at $\varepsilon > 40\%$–45% after the third cycle. Under compression at >45% strain, this result coincides well with both SEM results and conductivity under uniaxial compression in Figure 5. The cyclic stress–strain curves of rGO$_{hydro}$ and rGO$_{thermal}$ aerogels show a strain-hardening behavior, and no yield stress can be detected. This may indicate good stress transfer between the graphene sheets also at low density due to homogeneous structure and graphene–graphene joints. In the initial linear elastic region, both rGO$_{hydro}$ and rGO$_{thermal}$ aerogels gradually shrink, and the compressive stress slowly increases with the strain, which results from the elastic bending of the interconnected rGO pore structures.[36] Both rGO aerogels, the stress–strain curve in the second cycle is far more compliant than that observed in the first cycle; this effect is referred to as softening behavior (preconditioning effects).[37] The stable curves are typically observed after only three cycles. For the rGO$_{thermal}$ aerogel, the peak stress decreases by ≈11.5% in the first three cycles, while the rGO$_{hydro}$ aerogel decreases by ≈17.5%. Note that the stress–strain curve for rGO aerogels featured a plateau region followed by a steep region after the second cycle. In the plateau region, compressive stress gradually increased with the strain, indicating elastic deformation; in the steep regions, the stress increased rapidly with the strain owing to the densification of porous structures.[38] This is because the rGO$_{thermal}$ aerogel had few structural defects and a well-organized 3D network structure, which led to excellent compressive properties.
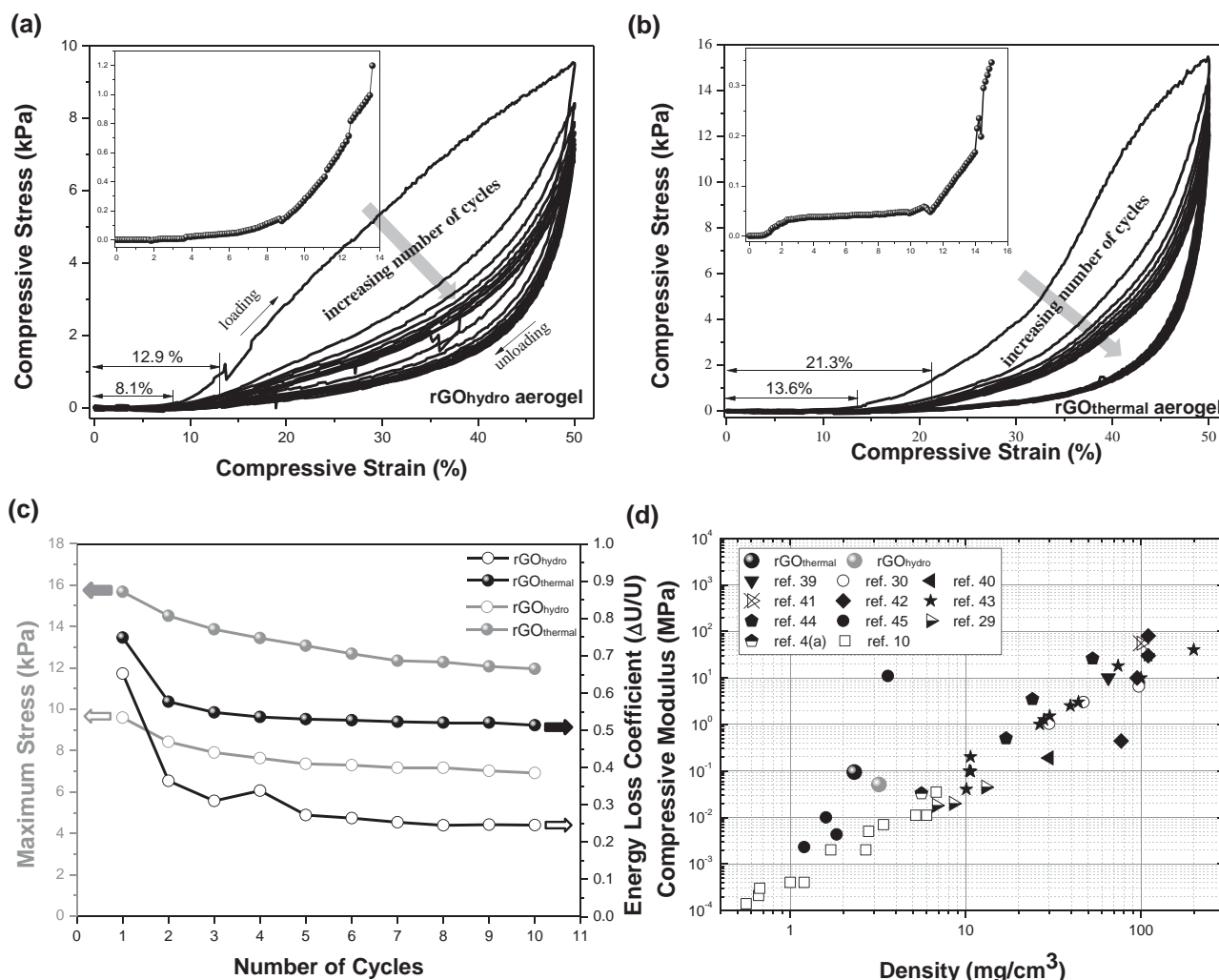
**ADVANCED
FUNCTIONAL
MATERIALS**
www.afm-journal.de

*Materials
Views*
www.MaterialsViews.com

**Figure 6.** a,b) Compressive stress–strain curves of rGO$_{hydro}$ ($r \approx 3.20$ mg cm$^{-3}$) and rGO$_{thermal}$ ($r \approx 2.32$ mg cm$^{-3}$) aerogel over 10 load–unload cycles. Compressive stress–strain curves of 10 cycles of loading–unloading (inset: magnified stress–strain curve in the region of low compressive strain). c) Maximum stress (left pointing arrows) and energy-loss coefficient (right pointing arrows) of rGO$_{thermal}$ aerogel during 10 cycles (calculated from the stress–strain curves shown in panel (a) and (b). d) The relationship between Young's modulus and bulk density as compared with other carbon-based aerogels.

Hysteresis behavior is very important in materials used for absorption.[4a,48–50] Hysteresis loops remain almost unchanged after the third cycle. The energy loss coefficient per cycle as a function of cycle number is plotted in Figure 6c for different values of compressive strain amplitude. Our rGO$_{thermal}$ aerogel exhibits excellent energy absorption capability. In Figure 6c, the energy loss coefficient of rGO$_{thermal}$ aerogel decreases from 74.9% to ≈54.8% in the first three cycles and then remains fairly constant. For all the rGO aerogels, a permanent plastic deformation is observed at the whole performance cycle. These results reflect during the measurements the damage of the inner structures.[51] The plastic deformation of the rGO$_{hydro}$ and rGO$_{thermal}$ aerogels only amounts to ≈12.9% and ≈21.3% of a residual strain after the 10 compression cycles, respectively, which corroborates the excellent structural robustness of the compressible rGO aerogel.[52] In comparison, the plastic deformation for polymeric foams at $\varepsilon \approx 20\%$ is typically 10%–30%, and nanotube-based foams usually have a plastic

deformation of 8%–20% with degradation under a compressive stress of 20%–30% at similar strain.[53] These results suggest that our aerogels are suitable for damping applications. The Young's modulus of the rGO$_{thermal}$ aerogel as a function of density is shown together with literature values for other 3D carbon-based aerogels in Figure 6d. The compressive modulus (94.5 kPa; $\rho \approx 2.32$ mg cm$^{-3}$) of the rGO$_{thermal}$ aerogel was higher at $\varepsilon = 50\%$ than that of other carbon-based aerogels.[54]

## 3. Conclusion

In summary, we prepared N-doped rGO aerogels exhibiting high electrical conductivities and compressibility by a combined method of hydrothermal and thermal annealing. These unique ultralow-density rGO aerogels provide both a porous graphene 3D network and good electrical and mechanical properties. This synthetic method provides fundamental insights

www.MaterialsViews.com

ADVANCED
FUNCTIONAL
MATERIALS
www.afm-journal.de

FULL PAPER

for further design and construction of other 3D layered hybrid aerogel materials for energy storage, photocatalysis, environmental protection, energy absorption, and sensing applications.

## 4. Experimental Section

*Sample Preparation*: GO (highly concentrated GO dispersion in water, Graphene Supermarket) and HMTA (Sigma-Aldrich) were used as received. In the hydrothermal method, the GO solution (1 mL) and HMTA (15 mg) were dissolved in deionized water (0.5 mL, $\geq$ 18 M$\Omega$ cm) in a vial (5 cc). The vial was sealed and then sonicated for 5 min. Hydrothermal treatment of the mixed solution was conducted at 110 °C for 8 h in an autoclave. Then, the autoclave was naturally cooled to room temperature and the product was removed. The rGO hydrogel was carefully washed using deionized water several times and then lyophilized (at −55 °C for 2 d) to remove the rGO$_{hydro}$ aerogel. Finally, the rGO$_{thermal}$ aerogel was obtained by annealing the rGO$_{hydro}$ aerogel in a tubular furnace at 1000 °C for 3 h at a rate of 1 °C min$^{-1}$ under vacuum ($10^{-3}$ Torr).

*General Characterization*: XRD patterns were collected on a Rigaku diffractometer using Cu K$\alpha$ radiation. Raman spectra were measured on a LabRam Aramis Raman spectrometer from Horiba Jobin Yvon. The instrument was fitted with a 532 nm laser. Samples were measured at room temperature using the microscope accessory with a 50× aperture using at least 100 scans. All XPS measurements were obtained using a SIGAM PROBE (ThermoVG) with a monochromatic Al K$\alpha$ X-ray source at 100 W. The microstructure was observed by field-emission SEM (JSM-6701F/INCA Energy, JEOL). Contact angles were measured using a Dataphysics Model OCA 15EC at six different points. Specific surface area and pore-size distribution were measured using a BET–BJH test. This study was performed in a Minisorp II BEL-Japan with an activation temperature of 150 °C in a vacuum. The sample was first conditioned isothermally at 77 K for 24 h. The Langmuir adsorption equation was used for analysis. Electrical conductivity was measured using a four-probe method. To optimize the electrical contact between copper foils and the rGO aerogel, both ends of the aerogel were carefully coated with a thin layer of silver paste. The electrical conductivity was measured with R-CHEK (model RC2175, see Figure S6 in the Supporting Information). Compressive strength was measured on cylindrical specimens ≈7 mm in height × 8 mm in diameter using a Lloyd LR10K plus mechanical tester with a crosshead speed of 2.0 mm min$^{-1}$. The compressive strength was calculated from the maximum load registered during the test divided by the original area.

## Supporting Information

Supporting Information is available from the Wiley Online Library or from the author.

## Acknowledgements

[1] Z. Chen, W. Ren, L. Gao, B. Liu, S. Pei, H.-M. Cheng, *Nat. Mater.* **2011**, *10*, 424.

[2] a) Y. Xu, K. Sheng, C. Li, G. Shi, *ACS Nano* **2010**, *4*, 4324; b) H. Bi, X. Xie, K. Yin, Y. Zhou, S. Wan, L. He, F. Xu, F. Banhart, L. Sun, R. S. Ruoff, *Adv. Funct. Mater.* **2012**, *22*, 4421.

[3] a) Y. Xu, Z. Lin, X. Huang, Y. Liu, Y. Huang, X. Duan, *ACS Nano* **2013**, *7*, 4042; b) Y. He, W. Chen, X. Li, Z. Zhang, J. Fu, C. Zhao, E. Xie, *ACS Nano* **2013**, *7*, 174; c) J.-L. Shi, W.-C. Du, Y.-X. Yin, Y.-G. Guo, L.-J. Wan, *J. Mater. Chem. A* **2014**, *2*, 10830; d) Z.-S. Wu, K. Parvez, X. Feng, K. Müllen, *Nat. Commun.* **2013**, *4*, 2487; e) M. F. El-Kady, R. B. Kaner, *Nat. Commun.* **2013**, *4*, 1475; f) W. Gao, N. Singh, L. Song, Z. Liu, A. L. M. Reddy, R. Ci, R. Vajtai, Q. Zhang, B. Wei, P. M. Ajayan, *Nat. Commun.* **2011**, *6*, 496; g) X. Peng, L. Peng, C. Wu, Y. Xie, *Chem. Soc. Rev.* **2014**, *43*, 3303; h) Z. Wei, D. Wang, S. Kim, S.-Y. Kim, Y. Hu, M. K. Yakes, A. R. Laracuente, Z. Dai, S. R. Marder, C. Berger, W. P. King, W. A. de Heer, P. E. Sheenhan, E. Riedo, *Science* **2010**, *328*, 1373; i) G. Xie, K. Zhang, B. Guo, Q. Liu, L. Fang, J. R. Gong, *Adv. Mater.* **2013**, *25*, 3820; j) S. Chen, S.-Z. Qiao, *ACS Nano* **2013**, *7*, 10190; k) A. J. Smith, Y.-H. Chang, K. Raidongia, T.-Y. Chen, L.-J. Li, J. Huang, *Adv. Energy Mater.* **2014**, *4*, 1400398; l) C. Hu, G. Zheng, F. Zhao, H. Shao, Z. Zhang, N. Chen, L. Jiang, L. Qu, *Energy Environ. Sci.* **2014**, *7*, 3699.

[4] a) H. Hu, Z. Zhao, W. Wan, Y. Gogotsi, J. Qiu, *Adv. Mater.* **2013**, *25*, 2219; b) C. Zhu, Y.-J. Han, E. B. Duoss, A. M. Golobic, J. D. Kuntz, C. M. Spadaccini, M. A. Worsley, *Nat. Commun.* **2014**, *6*, 6962; c) J. Li, J. Li, H. Meng, S. Xie, B. Zhang, L. Li, H. Ma, J. Zhang, M. Yu, *J. Mater. Chem. A* **2014**, *2*, 2934; d) L. Wang, Y. Huang, C. Li, J. Chen, X. Sun, *Phys. Chem. Chem. Phys.* **2015**, *17*, 2228.

[5] a) F. Yavari, Z. Chen, A. V. Thomas, W. Ren, H.-M. Cheng, N. Koratkar, *Sci. Rep.* **2011**, *1*, 166; b) L. Li, S. He, M. Liu, C. Zhang, W. Chen, *Anal. Chem.* **2014**, *87*, 1638.

[6] a) X. Xu, H. Li, Q. Zhang, H. Hu, Z. Zhao, J. Li, J. Li, Y. Qiao, Y. Gogotsi, *ACS Nano* **2015**, *9*, 3969; b) R. T. Olsson, M. A. S. Azizi Samir, G. Salazar-Alvarez, L. Belova, V. Ström, L. A. Berglund, O. Ikkala, J. Nogués, U. W. Gedde, *Nat. Nanotechnol.* **2010**, *5*, 584.

[7] a) Z. Xue, Y. Cao, N. Liu, L. Feng, L. Jiang, *J. Mater. Chem. A* **2014**, *2*, 2445; b) W. Liu, Y. Wang, Z. Li, *Chem. Commun.* **2014**, *50*, 10311; c) L. Jiang, Z. Fan, *Nanoscale* **2014**, *6*, 1922; d) Y. Tao, X. Xie, W. Lv, D.-M. Tang, D. Kong, Z. Huang, H. Nishihara, T. Ishii, B. Li, D. Golberg, F. Kang, T. Kyotani, Q.-H. Yang, *Sci. Rep.* **2013**, *3*, 2975.

[8] a) S. Nardecchia, D. Carriazo, M. L. Ferrer, M. C. Gutiérrez, F. del Monte, *Chem. Soc. Rev.* **2013**, *42*, 794; b) Z. Zhao, X. Wang, J. Qiu, J. Lin, D. Xu, C. Zhang, M. Lv, X. Yang, *Rev. Adv. Mater. Sci.* **2014**, *36*, 137; c) X. Wang, G. Sun, P. Chen, *Front. Energy Res.* **2014**, DOI: 10.3389/fenrg.2014.00033.

[9] M. B. Bryning, D. E. Milkie, M. F. Islam, L. A. Hough, J. M. Kikkawa, A. G. Yodh, *Adv. Mater.* **2007**, *19*, 661.

[10] L. Qiu, J. Z. Liu, S. L. Y. Chang, Y. Wu, D. Li, *Nat. Commun.* **2012**, *3*, 1241.

[11] Y. Zhao, J. Liu, Y. Hu, H. Cheng, C. Hu, C. Jiang, L. Jiang, A. Cao, L. Qu, *Adv. Mater.* **2013**, *25*, 591.

[12] Y. Wu, N. Yi, L. Huang, T. Zhang, S. Fang, H. Chang, N. Li, J. Oh, J. A. Lee, M. Kozlov, A. C. Chipara, H. Terrones, P. Xiao, G. Long, Y. Huang, F. Zhang, X. Lepró, C. Haines, M. D. Lima, N. R. Lopez, L. P. Rajukumar, A. L. Elisa, S. Feng, S. J. Kim, N. T. Narayanan, P. M. Ajayan, M. Terrones, A. Aliev, P. Chu, Z. Zhang, R. H. Baughman, Y. Chen, *Nat. Commun.* **2014**, *6*, 6141.

[13] a) C. Zhu, T. Y.-J. Han, E. B. Duoss, A. M. Golobic, J. D. Kuntz, C. M. Spadaccini, M. A. Worsley, *Nat. Commun.* **2015**, *6*, 6962; b) H. Ha, K. Shanmuganathan, C. J. Ellison, *ACS Appl. Mater. Interfaces* **2015**, *7*, 6220; c) Q. Fang, B. Chen, *J. Mater. Chem. A* **2014**, *2*, 8941.

[14] J. W. Lee, J. M. Ko, J.-D. Kim, *J. Phys. Chem. C* **2011**, *115*, 19445.

[15] a) X. Fan, W. Peng, Y. Li, X. Li, S. Wang, G. Zhang, F. Zhang, *Adv. Mater.* **2008**, *20*, 4490; b) C. Chen, W. Kong, H.-M. Duan, J. Zhang, *Phys. Chem. Chem. Phys.* **2014**, *16*, 12858.

[16] a) Z. Lei, X. S. Zhao, *Energy Environ. Sci.* **2012**, *5*, 6391; b) L. Lai, L. Chen, D. Zhan, L. Sun, J. Liu, S. H. Lim, C. K. Poh, Z. Shen, J. Lin, *Carbon* **2011**, *49*, 3250.

[17] D. Li, M. B. Müller, S. Gilje, R. B. Kaner, G. G. Wallace, *Nat. Nanotechnol.* **2008**, *3*, 101.

[18] a) Q. Kang, J. T. W. Yeow, R. Barnett, *Carbon* **2012**, *50*, 2201; b) V. K. Singh, M. K. Patra, M. Manoth, G. S. Gowd, S. R. Vadera, N. Kumar, *New Carbon Mater.* **2009**, *24*, 147.

[19] S. Park, J. An, J. R. Potts, A. Velamakanni, S. Murali, R. S. Ruoff, *Carbon* **2011**, *49*, 3019.

[20] K. N. Kudin, B. Ozbas, H. C. Schniepp, R. K. Prud'homme, I. A. Aksay, R. Car, *Nano Lett.* **2008**, *8*, 36.

[21] a) H. Wang, T. Maiyalagan, X. Wang, *ACS Catal.* **2012**, *2*, 781; b) X. Li, H. Wang, J. T. Robinson, H. Sanchez, G. Diankov, H. Dai, *J. Am. Chem. Soc.* **2009**, *131*, 15939; c) D. Wei, Y. Liu, Y. Wang, H. Zhang, L. Huang, G. Yu, *Nano Lett.* **2009**, *9*, 1752.

[22] F. Tuinstra, J. L. Koenig, *J. Chem. Phys.* **1970**, *53*, 1126.

[23] D. Deng, X. Pan, L. Yu, Y. Cui, Y. Jiang, J. Qi, W.-X. Li, Q. Fu, X. Ma, Q. Xue, G. Sun, X. Bao, *Chem. Mater.* **2011**, *23*, 1188.

[24] L. Wang, Z. Sofer, J. Luxa, M. Pumera, *J. Mater. Chem. C* **2014**, *2*, 2887.

[25] a) L. Lai, J. R. Potts, D. Zhan, L. Wang, C. K. Poh, C. Tang, H. Gong, Z. Shen, J. Lin, R. S. Ruoff, *Energy. Environ. Sci.* **2012**, *5*, 7936; b) S. van Dommele, A. Romero-Izquirdo, R. Brydson, K. P. de Jong, J. H. Bitter, *Carbon* **2008**, *1*, 138; c) H. Chen, Y. Yang, Z. Hu, K. Huo, Y. Ma, Y. Chen, *J. Phys. Chem. B* **2006**, *110*, 16422; d) D. H. Lee, W. J. Lee, S. O. Kim, *Nano Lett.* **2009**, *9*, 1427; e) S. Schelm, G. B. Smith, *J. Phys. Chem. B* **2005**, *109*, 1689.

[26] a) N. Li, Z. Wang, K. Zhao, Z. Shi, Z. Gu, S. Xu, *Carbon* **2010**, *48*, 255; b) Y. Wang, Y. Shao, D. W. Matson, J. Li, Y. Lin, *ACS Nano* **2010**, *4*, 1790; c) N. P. Subramanian, X. Li, V. Nallathambi, S. P. Kumaraguru, H. Colon-Mercado, G. Wu, J.-W. Lee, B. N. Popov, *J. Power Sources* **2009**, *188*, 38.

[27] H. Tang, P. Gao, Z. Bao, B. Zhou, J. Shen, Y. Mei, G. Wu, *Nano Res.* **2015**, DOI:10.1007/s12274-014-0672-z.

[28] M. A. Worsley, P. J. Pauzauskie, T. Y. Olson, J. Biener, J. H. Satcher Jr., T. F. Baumann, *J. Am. Chem. Soc.* **2010**, *132*, 14067.

[29] H. Sun, Z. Xu, C. Gao, *Adv. Mater.* **2013**, *25*, 2554.

[30] X. Zhang, Z. Sui, B. Xu, S. Yue, Y. Luo, W. Zhan, B. Liu, *J. Mater. Chem.* **2011**, *21*, 6494.

[31] J. Zou, J. Liu, A. S. Karakoti, A. Kumar, D. Joung, Q. Li, S. I. Khondaker, S. Seal, L. Zhai, *ACS Nano* **2010**, *4*, 7293.

[32] K. H. Kim, Y. Oh, M. F. Islam, *Nat. Nanotechnol.* **2012**, *7*, 562.

[33] H. Bi, K. Yin, X. Xie, Y. Zhou, N. Wan, F. Xu, F. Banhart, L. Sun, R. S. Ruoff, *Adv. Mater.* **2012**, *24*, 5124.

[34] P. Hagenmuller, G. Chambon, M. Naaim, *Cryosphere Discuss.* **2015**, *9*, 1425.

[35] J.H. Rhee, C.-C. Chung, E. W.-G. Diau, *NPG Asia Mater.* **2012**, *4*, e68.

[36] a) C. Wang, X. He, Y. Shang, Q. Peng, Y. Qin, E. Shi, Y. Yang, S. Wu, W. Xu, S. Du, A. Cao, Y. Li, *J. Mater. Chem. A* **2014**, *2*, 14994; b) C. Zhu, Y.-J. Han, E. B. Duoss, A. M. Golobic, J. D. Kuntz, C. M. Spadaccini, M. A. Worsley, *Nat. Commun.* **2015**, *6*, 6962; c) S. Yang, L. Chen, L. Mu, B. Hao, P.-C. Ma, *RSC Adv.* **2015**, *5*, 38470; d) Z. Lin, X. Gui, Q. Gan, W. Chen, X. Cheng, M. Liu, Y. Zhu, Y. Yang, A. Cao, Z. Tang, *Sci. Rep.* **2015**, *5*, 11336.

[37] a) J. Suhr, P. Victor, L. Ci, S. Sreekala, X. Zhang, O. Nalamasu, P. M. Ajayan, *Nat. Nanotechnol.* **2007**, *2*, 417; b) L. Liu, W. Ma, Z. Zhang, *Small* **2011**, *7*, 1504; c) M. Karakay, D. Saini, R. Podila, M.J. Skove, A. M. Rao, R. Thevamaran, C. Daraio, *Adv. Eng. Mater.* **2015**, *17*, 990.

[38] H.-W. Liang, Q.-F. Guan, L.-F. Chen, Z. Zhu, W.-J. Zhang, S.-H. Yu, *Angew. Chem.* **2012**, *51*, 5101.

[39] M. A. Worsley, S. Charnvanichborikarn, E. Montalvo, S. J. Shin, E. D. Tylski, J. P. Lewicki, A. J. Nelson, J. H. Satcher Jr., J. Biener, T. F. Baumann, S. O. Kucheyev, *Adv. Funct. Mater.* **2014**, *24*, 4259.

[40] Z. Tang, S. Shen, J. Zhuang, X. Wang, *Angew. Chem. Int. Ed.* **2010**, *49*, 4603.

[41] M. A. Worsely, S. O. Kucheyev, H. E. Mason, M. D. Merrill, B. P. Mayer, J. Lewicki, C. A. Valdez, M. E. Suss, M. Stadermann, P. J. Pauzauskie, J. H. Satcher Jr., J. Biener, T. F. Baumann, *Chem. Commun.* **2012**, *48*, 8428.

[42] R. W. Pekala, C. T. Alviso, J. D. LeMay, *J. Non-Cryst. Solids* **1990**, *125*, 67.

[43] M. A. Worsley, S. O. Kucheyev, J. H. Satcher Jr., A. V. Hamza, T. F. Baumann, *Appl. Phys. Lett.* **2009**, *94*, 073115.

[44] Y. Li, J. Chen, L. Huang, C. Li, J.-D. Hong, G. Shi, *Adv. Mater.* **2014**, *26*, 4789.

[45] H. Sun, Z. Xu, C. Gao, *Adv. Mater.* **2013**, *25*, 2554.

[46] H. Hu, Z. Zhao, W. Wan, Y. Gogotsi, J. Qiu, *Adv. Mater.* **2013**, *25*, 2219.

[47] L. Qiu, J. Z. Liu, S. L. Y. Chang, Y. Wu, D. Li, *Nat. Commun.* **2012**, *3*, 1241.

[48] H.-W. Liang, Q.-F. Guan, L.-F. Chen, Z. Zhu, W.-J. Zhang, S.-H. Yu, *Angew. Chem. Int. Ed.* **2012**, *124*, 5191.

[49] T. A. Schaedler, A. J. Jacobsen, A. Torrents, A. E. Sorensen, J. Lian, J. R. Greer, L. Valdevit, W. B. Carter, *Science* **2011**, *334*, 962.

[50] A. Cao, P. L. Dickrell, W. G. Sawyer, M. N. Ghasemi-Nejhad, P. M. Ajayan, *Science* **2005**, *310*, 1307.

[51] X. Xie, Y. Zhou, H. Bi, K. Yin, S. Wan, L. Sun, *Sci. Rep.* **2013**, *3*, 2117.

[52] H.-W. Liang, Q.-F. Guan, L.-F. Chen, Z. Zhu, W.-J. Zhang, S.-H. Yu, *Angew. Chem.* **2015**, *54*, 2397.

[53] X. Wang, L.-L. Lu, Z.-L. Yu, X.-W. Xu, Y.-R. Zheng, S.-R. Yu, *Angew. Chem.* **2015**, *54*, 2397.

[54] a) X. Yao, W. Yu, X. Xu, F. Chen, Q. Fu, *Nanoscale* **2015**, *7*, 3959; b) Y. Li, J. Chen, L. Huang, C. Li, J.-D. Hong, G. Shi, *Adv. Mater.* **2014**, *26*, 4789.